



# Impacts of estimated plume rise on PM<sub>2.5</sub> exceedance prediction during extreme wildfire events: A comparison of three schemes (Briggs, Freitas, and Sofiev)

Yunyao Li<sup>1,2</sup>, Daniel Tong<sup>1,2,3</sup>, Siqi Ma<sup>1,2</sup>, Saulo R. Freitas<sup>4</sup>, Ravan Ahmadov<sup>5,6</sup>, Mikhail Sofiev<sup>7</sup>,  
5 Xiaoyang Zhang<sup>8</sup>, Shobha Kondragunta<sup>9</sup>, Ralph Kahn<sup>10</sup>, Youhua Tang<sup>2,3</sup>, Barry Baker<sup>3</sup>, Patrick  
Campbell<sup>3</sup>, Rick Saylor<sup>3</sup>, Georg Grell<sup>11</sup>, Fangjun Li<sup>8</sup>

<sup>1</sup>Department of Atmospheric, Oceanic and Earth Sciences, George Mason University, Fairfax, VA22030, USA

<sup>2</sup>Center for Spatial Information Science and Systems, George Mason University, Fairfax, VA 22030, USA

<sup>3</sup>Air Resources Laboratory, National Oceanic and Atmospheric Administration, College Park, MD 20740, USA

10 <sup>4</sup>Center for Weather Forecasting and Climate Studies, National Institute for Space Research, São José dos Campos, 12227, Brazil

<sup>5</sup>Cooperative Institute for Research in Environmental Sciences, University of Colorado at Boulder, Boulder, CO 80305, USA

<sup>6</sup>Global Systems Laboratory, National Oceanic and Atmospheric Administration, Boulder, CO 80305, USA

<sup>7</sup>Atmospheric Composition Research, Finnish Meteorological Institute, Helsinki, 00101, Finland

15 <sup>8</sup>Geospatial Sciences Center of Excellence, Department of Geography & Geospatial Sciences, South Dakota State University, Brookings, 57007, USA

<sup>9</sup>Satellite Meteorology and Climatology Division, National Oceanic and Atmospheric Administration, College Park, MD 20740, USA

<sup>10</sup>National Aeronautics and Space Administration Goddard Space Flight Center, Greenbelt, 20771, USA

20 <sup>11</sup>Global Systems Laboratory, National Oceanic and Atmospheric Administration, Boulder, CO 80305, USA

*Correspondence to:* Yunyao Li ([yli74@gmu.edu](mailto:yli74@gmu.edu)), Daniel Tong ([qtong@gmu.edu](mailto:qtong@gmu.edu))

**Abstract.** Plume height plays a vital role in wildfire smoke dispersion and the subsequent effects on air quality and human health. In this study, we assess the impact of different plume rise schemes on predicting the dispersion of wildfire air pollution, and the exceedances of the National Ambient Air Quality Standards (NAAQS) for fine particulate matter (PM<sub>2.5</sub>) during the  
25 2020 Western United States Wildfire season. Three widely used plume rise schemes (Briggs 1969, Freitas 2007, Sofiev 2012) are compared within the Community Multiscale Air Quality (CMAQ) modelling framework. The plume heights simulated by these schemes are comparable to the aerosol height observed by the Multi-angle Imaging SpectroRadiometer (MISR). The performance of the simulations with these schemes varies by fire case and weather conditions. On average, simulations with higher plume injection heights predict lower AOD and surface PM<sub>2.5</sub> concentrations near the source region but higher AOD  
30 and PM<sub>2.5</sub> in downwind regions due to the faster spread of the smoke plume once ejected. The two-month mean AOD difference caused by different plume rise schemes is approximately 20-30% near the source regions and 5-10% in the downwind regions. Thick smoke blocks sunlight and suppresses photochemical reactions in areas with high AOD. The surface PM<sub>2.5</sub> difference reaches 70% on the west coast and the difference is lower than 15% in the downwind regions. Moreover, the plume injection height affects pollution exceedance (>35 µg/m<sup>3</sup>) forecasts. Higher plume heights generally produce larger downwind PM<sub>2.5</sub>  
35 exceedance areas. The PM<sub>2.5</sub> exceedance areas predicted by the three schemes largely overlap, suggesting that all schemes



perform similarly during large wildfire events when the predicted concentrations are well above the exceedance threshold. At the edges of the smoke plumes, however, there are noticeable differences in the  $PM_{2.5}$  concentration and predicted  $PM_{2.5}$  exceedance region. This disagreement among the  $PM_{2.5}$  exceedance forecasts may affect key decision-making regarding early warning of extreme air pollution episodes at local levels during large wildfire events.



## 1 Introduction

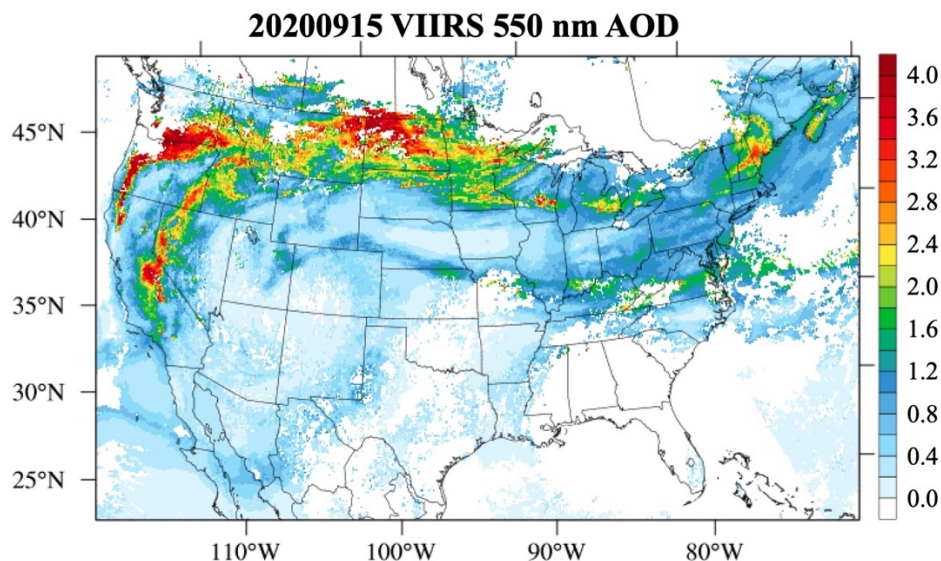
Wildfires release large amounts of aerosol and trace gases into the atmosphere, which degrades the air quality and adversely affects human health (Koning et al., 1985). Previous studies (Reid et al., 2016; Cascio, 2018) have demonstrated that a strong association exists between exposure to wildfire smoke and all-cause mortality and respiratory morbidity. The global average annual mortality attributable to landscape fire smoke exposure was estimated at 339,000 deaths annually (Johnston et al., 2012). O’Neil et al. (2021) discuss the regional health impacts of the 2017 Northern California wildfires and estimated 83 excess deaths from exposure to PM<sub>2.5</sub> (particulate matter less than 2.5 µm in diameter), of which 47% were attributable to wildfire smoke during the smoke episode. Liu et al. (2021) assessed the health impact of the 2020 Washington State wildfire smoke episode, which caused 38.4 more all-causes mortality cases and 15.1 more respiratory mortality cases. Aerosols emitted from wildfires also affect photolysis rates and photochemistry (Tang et al., 2003) as well as ozone photochemical production (Val Martín et al., 2006; Akagi et al., 2013).

Previous studies have found that the smoke injection height plays a vital role in smoke dispersion, as wind speed and direction generally vary with altitude (e.g., Vernon et al., 2018). In addition, a higher injection height will reduce near-source concentration, increase downwind concentrations (Li et al., 2020), and can influence the removal processes and atmospheric lifetime of emitted particles and trace gases. Briggs (1969) introduced a set of semi-empirical formulas to estimate plume injection height for stack emissions from stationary power-plant point sources in different atmospheric stability states using buoyancy flux, horizontal wind speed, static stability, and atmospheric turbulence conditions. This scheme is widely used in dispersion models such as the National Oceanic and Atmospheric Administration (NOAA) Hybrid Single-Particle Lagrangian Integrated Trajectory model (HYSPPLIT; Draxler and Hess, 1998) and Community Multiscale Air Quality Modeling System (CMAQ; Byun and Schere, 2006). However, the Briggs scheme was not designed for irregular large point sources, such as forest fires, and some of the input parameters, such as heat flux, are difficult to obtain. Freitas et al. (2007) developed a 1-D plume rise and transport parameterization for low-resolution atmospheric chemistry models, which was built upon governing equations for the first law of thermodynamics, vertical motion, and continuity for the water phases. Sofiev et al. (2012) developed a new plume rise scheme, which utilizes fire radiative power (FRP), planetary boundary layer (PBL) height, and the Brunt-Vaisala frequency in the free troposphere to estimate the plume injection height from wildfires. The parameters of the new scheme were determined using the plume height observations collected by the Multi-angle Imaging SpectroRadiometer (MISR) Plume Height Project in North America (Val Martín et al., 2010) and Siberia. The plume height estimation in models is of great uncertainty. Ye et al. (2021) compared the calculated plume heights from 12 state-of-the-art air quality forecasting systems during the Williams Flats fire in Washington State, US, August 2019, during the Fire Influence on Regional to Global Environments and Air Quality (FIREX-AQ) field campaign, and found that there was a large spread of the modelled plume heights.



75 In the summer and early autumn of 2020, the western United States (U.S.) experienced a record-breaking wildfire season. A  
series of large wildfires fuelled by accumulated biomass, heatwaves, and dry winds, burned more than 10 million acres. From  
late August to early October 2020, the West Coast wildfires contributed 23% of surface  $PM_{2.5}$  pollution nationwide and caused  
3,720 observed  $PM_{2.5}$  exceedances (Li et al., 2021). The thick fire smoke that originated in California, Oregon, and Washington  
was injected into the free troposphere and transported across the country through the prevailing wind, which caused hazy days  
80 in 19 states (Figure 1).

This study aims to evaluate the impact of different plume rise schemes on aerosol distribution and photochemistry during the  
2020 record-breaking wildfire season. We use the George Mason University (GMU) wildfire forecast system (Li et al., 2021)  
that relies on satellite estimates of biomass burning emissions and the CMAQ to simulate the emission, transport, and  
85 transformation of smoke during the 2020 summer wildfire season. Three plume rise schemes are used: Briggs (1969), Freitas  
(2007), and Sofiev (2012). The Briggs (1969) scheme was implemented in the standard release of the CMAQ version. Li et al.  
(2021) implemented the Sofiev scheme into CMAQ, and in this work, the Freitas scheme is also implemented. The plume  
injection height's impact on  $PM_{2.5}$  distribution is evaluated in section 3. Its impact on aerosol optical depth (AOD) is shown  
in section 4. Finally, we discuss the plume rise impact on photochemistry in section 5.



90

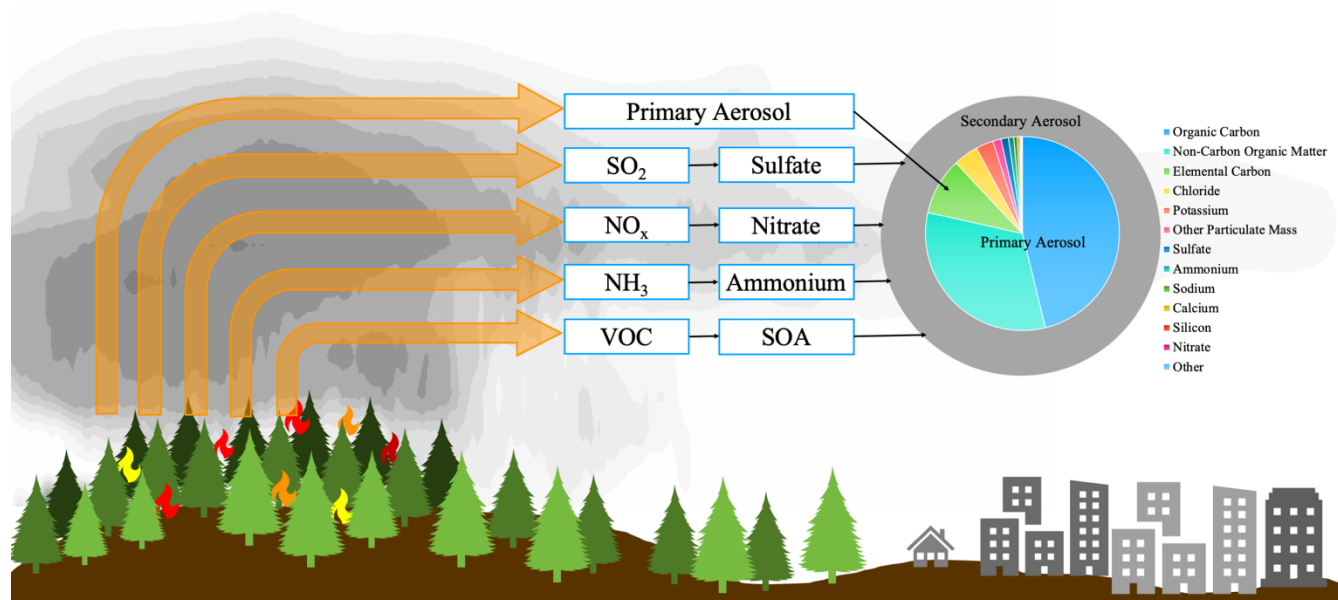
**Figure 1. The Visible Infrared Imaging Radiometer Suite (VIIRS) measured 550 nm aerosol optical depth (AOD) on September 15, 2020, over the continental United States.**



## 2 Methods

### 2.1 Experiment Design

95 Biomass burning is an important source of global aerosols that have a great impact on air quality. Figure 2 shows how wildfire smoke affects local and downwind air quality. The wildfire emissions include primary aerosols and large amounts of gases that can be oxidized to form secondary aerosols. In the biomass burning input of our model, the major components of the primary aerosols are organic carbon, non-carbon organic matter, elemental carbon, chloride, and potassium. The other wildfire emissions like  $\text{SO}_2$ ,  $\text{NO}_x$  ( $\text{NO}+\text{NO}_2$ ),  $\text{NH}_3$ , and VOCs may form secondary aerosols such as sulfate, nitrate, ammonium, and secondary organic aerosols (SOA) after being emitted. The temporal and spatial impacts of plume rise on different primary or  
100 secondary aerosol species may be different, as the generation of the secondary aerosols usually takes time. The difference in the dispersion of primary and secondary aerosols will contribute to further differences in photochemistry and health impacts. Therefore, it is important to discuss the impact of plume rise on each primary and secondary aerosol species.



105 **Figure 2: Wildfire primary emissions and downwind evolution.**

To evaluate the impact of different plume rise schemes on aerosol dispersion and photochemistry modelling during the 2020 recording-breaking wildfire season, four CMAQ simulations were conducted. In the first run (B69), we used the CMAQ default plume rise scheme based on Briggs (1969). In the second run (F07), we implemented the Freitas et al. (2007) scheme into the  
110 CMAQ model and used it to calculate the plume injection height. In the third run (S12), we used the Sofiev et al. (2012) plume rise scheme as implemented in Li et al. (2021). In the fourth run (NoFire), we turned off all types of biomass burning emissions. Wildfire impact is represented by the difference between the simulation with fire and the NoFire run. More information on the



three plume rise schemes is provided in section 2.3. Besides the difference in the plume rise scheme, the setups for these three runs are the same. More details about the CMAQ setup are given in section 2.2. Comparing results from these three simulations  
115 elucidates the impacts of plume injection height predictions on the distribution of each aerosol species (section 3.2), AOD and photochemistry (section 3.3), as well as surface air quality and PM<sub>2.5</sub> exceedances (section 3.4).

## 2.2 Description of the Model System

The George Mason University (GMU) air quality modeling system was employed to simulate the 2020 summer wildfire season from August 1<sup>st</sup> to September 30<sup>th</sup>, 2020 over the contiguous United States (CONUS) domain. This system uses CMAQ  
120 Version 5.3.1 (U.S. EPA, 2020a) as the chemical transport model and the Weather Research and Forecasting (WRF; Skamarock et al., 2019) model V4.2 output as the meteorology inputs for the CMAQ model. The model domain is configured with 12 km by 12 km horizontal resolution and 35 vertical layers. The initial and boundary conditions for WRF are from the Global Data Assimilation System (GDAS) 0.25-degree analysis and forecast. The main physics choices were the Grell-Freitas scheme (Grell & Freitas, 2014) for parameterized cumulus processes, the Mellor-Yamada-Janjic scheme (Janjic, 1994) for  
125 planetary boundary layer (PBL) processes, the two-moment Morrison microphysics (Morrison et al., 2009) for cloud physics processes, the RRTMG scheme (Iacono et al., 2008) for longwave and shortwave radiation, and the Noah scheme (Koren et al., 1999) for land surface processes. The biomass burning emissions product used in this study is the 0.1 degree daily blended Global Biomass Burning Emissions Product from Moderate Resolution Imaging Spectroradiometer (MODIS) and Visible Infrared Imaging Radiometer Suite (VIIRS) (GBBEPx V3, Zhang, et al., 2012, 2019). The GBBEPx Fire radiative power  
130 (FRP) in the GBBEPx is averaged from observations from MODIS on Terra and Aqua MODIS and VIIRS M-band on Suomi National Polar-orbiting Partnership (SNPP) and the Joint Polar Satellite System-1 (JPSS) VIIRS. Anthropogenic emissions were prepared with the 2016v1 Emissions Modelling Platform, using the baseline emissions taken from the National Emissions Inventory (NEI) 2016 Collaborative (Eyth et al., 2020). We then shifted the base year emission to the prediction year 2020 using representative days of each month (U.S. EPA, 2020b). The model-ready emission files are processed and generated by  
135 the Sparse Matrix Operator Kernel Emissions (SMOKE) model (Houyoux et al., 2000) V4.7. The CB6 gas-phase chemical mechanism (Luecken et al., 2019), AE07 aerosol scheme (Pye et al., 2015; Xu et al., 2018), and aqueous chemistry (Fahey et al., 2017) is used in the CMAQ system. Details about the system setup are shown in Table S1 of Li et al. (2021).

The evaluation of the model performance with Sofiev et al. (2012) plume rise scheme has been discussed in Li et al. (2021).  
140 The averaged correlation between observed (from AirNow) and simulated daily PM<sub>2.5</sub> concentrations is 0.55. The averaged normalized mean error of the simulated surface PM<sub>2.5</sub> is 3.9% for the year 2020. The average area hit ratio for exceedances is 0.68 (Fig 2a from Li et al., 2021). A high area hit ratio represents a good capture of the region impacted by smoke. During the peak pollution days (from September 12<sup>th</sup> to 16<sup>th</sup>), the area hit ratios were higher than 0.96 with a maximum of 1.0 on September 13<sup>th</sup>, 2020. This suggests that the model could predict more than 96% of the observed exceedances when the smoke pollution  
145 was at its peak. Also, the simulated PM<sub>2.5</sub> vertical profiles in the West Coast and Central U.S. matched the Cloud-Aerosol





Lidar and Infrared Pathfinder Satellite Observations (CALIPSO) near the wildfire source region and downwind area (Fig S2 from Li et al., 2021). Overall, the model can reproduce wildfire smoke dispersion, especially when the smoke is thick.

### 2.3 Description of the plume rise schemes

The three schemes used in the current experiment are very different in their nature and underlying assumptions, but they all were developed with an individual fire as a model source of buoyancy and smoke. In this experiment, as well as in many other applications of these schemes, the input fire information is gridded with a grid cell size of several km or larger. Strictly speaking, such setup goes beyond the area of applicability of these schemes. However, with a growing number of gridded fire emission products and their applications for atmospheric composition and air quality tasks, it is important to evaluate this very setup – and to compare the robustness of these models to violation of their underlying assumptions. In this study, we use the default coefficient settings in each scheme. We did not tune the coefficient of any scheme to get the best simulation for any major fire case. Because the main focus of this study is to evaluate the impact of different plume injection heights on the near source and downwind air quality. The two-month average state is more important to our results and future health studies.

#### 2.3.1 Briggs scheme (B69)

The default plume rise scheme in CMAQ is based on Briggs (1969) and has been modified by revisions in Briggs (1971, 1972, 1984). It uses a set of semi-empirical formulas to estimate plume injection height in different atmospheric stability states. Heat flux, horizontal wind speed, static stability, and friction velocity are used to estimate the plume injection height. In this study, we derive the heat flux from FRP from the GBBEPx dataset multiplied by a factor of 10, following Val Martin et al. (2012). The Briggs scheme is widely used in chemical transport models; however, it was not designed for forest fires.

#### 2.3.2 Freitas scheme (F06)

Freitas et al. (2007) developed a 1-D plume rise and transport parameterization for low-resolution atmospheric chemistry models, which was built upon governing equations for the first law of thermodynamics, vertical motion, and continuity for the water phases (Eq. 1-5 from Freitas et al., 2007). The Freitas scheme is the default plume rise scheme in WRF-Chem and has been widely used in many studies. However, the Freitas scheme has never before been used with CMAQ. In this work, the FRP based Freitas scheme from High-Resolution Rapid Refresh Smoke (HRRR-Smoke; Ahmadov et al., 2017) model has been implemented into CMAQ. Wind, temperature, pressure, and humidity from WRFV4.2 meteorology inputs as well as FRP and fire size are used to calculate the plume injection height in the model. The FRP from GBBEPx and fire size from RAP-Chem (Archer-Nicholls et al., 2015) are used to calculate fire buoyancy in the model.

#### 2.3.3 Sofiev scheme (S12)

Sofiev et al. (2012) developed a new plume rise scheme that considers wildfire plumes in a way similar to Convective Available Potential Energy (CAPE) computations. It utilizes FRP, PBL height, and the Brunt-Vaisala frequency from WRFV4.2 in the



free troposphere to estimate the plume injection height from wildfires (Eq. 10-11 from Sofiev et al., 2012). In our previous study, we added the Sofiev scheme to CMAQ (Li et al., 2021) and have applied it previously to predict air quality during the 2020 wildfire season.

## 2.4 Observation data

### 180 2.4.1 MISR plume height observation

The predicted plume height is evaluated using observations from Multi-angle Imaging SpectroRadiometer (MISR) space-based, multi-angle stereo imaging. The MISR instrument obtains imagery of each location within its 380 km-wide swath at nine view angles, ranging from 70 forward, through nadir, to 70 aft, along the orbit track, in each of four spectral bands centered at 446 (blue), 558 (green), 672 (red), and 866 nm (near-infrared) wavelengths (Diner et al., 1998). MISR is in a sun-  
185 synchronous orbit, crossing the Equator at approximately 10:30 AM local time, so observations in the study region occurred in the mid-to-late morning. The MISR INteractive eXplorer (MINX) software is used in this study to derive plume heights from MISR imagery (Nelson et al., 2013; Val Martin et al., 2018). The MINX wind-corrected plume height information is then used to evaluate the simulated plume height in this paper.

### 190 2.4.2 AirNow surface PM<sub>2.5</sub> data

The hourly ground PM<sub>2.5</sub> observations from the U.S. EPA AirNow network (<https://files.airnowtech.org/?prefix=airnow>) are used to evaluate the surface air pollution predictions in this study. The real-time AirNow measurements are collected by the state, local, or tribal environmental agencies using federal references or equivalent monitoring methods approved by EPA. It contains the air quality data for more than 500 cities across the U.S., as well as for Canada and Mexico.

## 195 3 Results

### 3.1 Comparing simulated plume heights against MISR observations

The simulated net plume heights (removing terrain elevation) from three simulations: B69, F07, and S12 are compared with MISR observations for the Milepost 21 Fire on August 15<sup>th</sup>, 2020, and the August Complex Fire on August 31<sup>st</sup>, 2020 (Figure 3). The performance of different schemes varies by fire cases and weather conditions. For the Milepost 21 Fire, the plume  
200 heights simulated by B69 and S12 are similar, but lower than that by F07. In the case of the August Complex Fire, the plume heights simulated by B69 are higher than that by F07 and S12. Previous studies found that for the large fires injected above the PBL, the plume height calculated by S12 is less sensitive to FRP than by B69 (Li et al., 2020). Some of the fire points during the August Complex Fire had higher FRP than that during the Milepost 21 Fire, so the estimated plume height by B69 is higher than that by S12. For the F07 scheme, the plume injection height is higher when it is wetter (Freitas et al., 2007). The  
205 water vapor mixing ratio on August 15<sup>th</sup> is higher than on August 31<sup>st</sup>, which contributes to the higher plume height during the

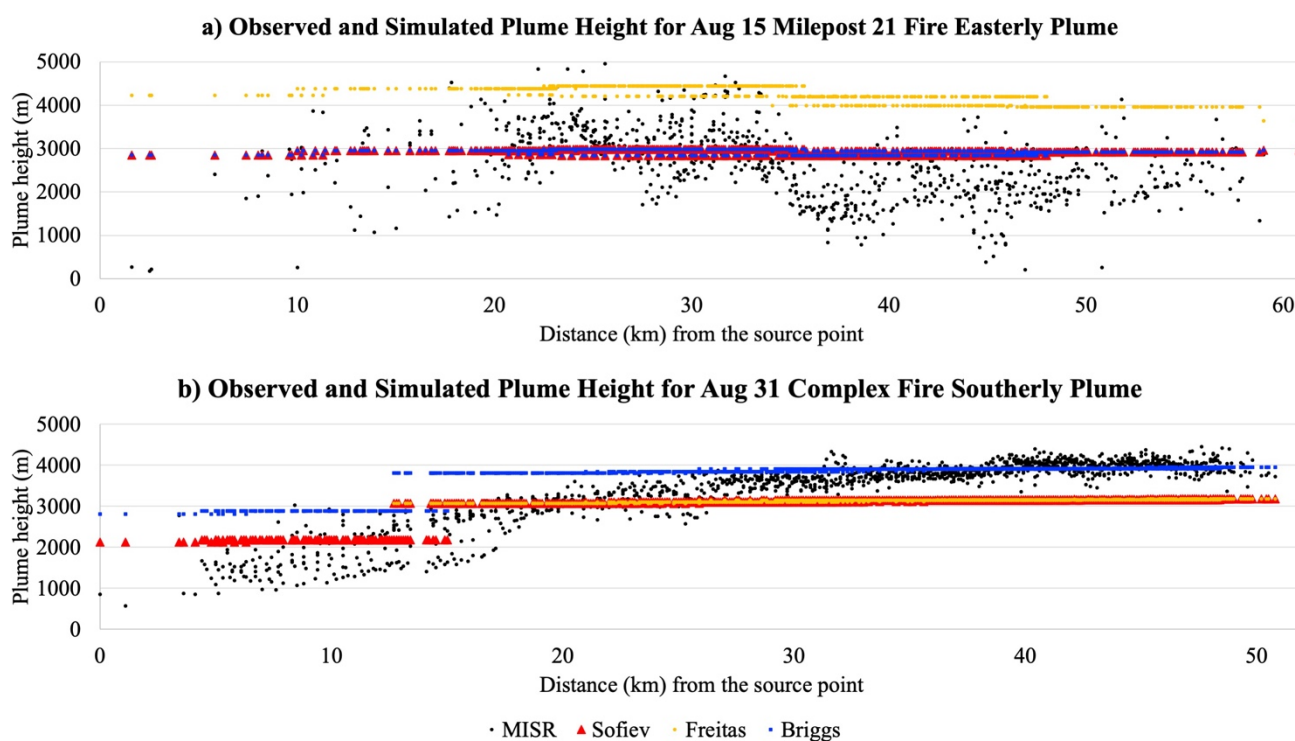




Milepost 21 Fire than during the August Complex fire. Overall, the simulated plume heights with all three schemes are reasonably comparable to the MISR observations.

Another possible reason for B69 showing higher injection than two other schemes is the higher power of the buoyancy flux in neutral and unstable PBL, combined with the gridded representation of fires. Indeed, for neutral and unstable ABL, B69 suggest

210 the injection height proportional to buoyancy flux to the power of  $3/4$  or  $4/5$ , depending on wind speed. As a result, these formulations appear sensitive to summation of all fires over a grid cell into a single “gridded fire”, with the energy release being a sum of all fires. In S12, for instance, the analogous power is always  $1/3$ , which makes that scheme less sensitive to the gridded fire representation.



215

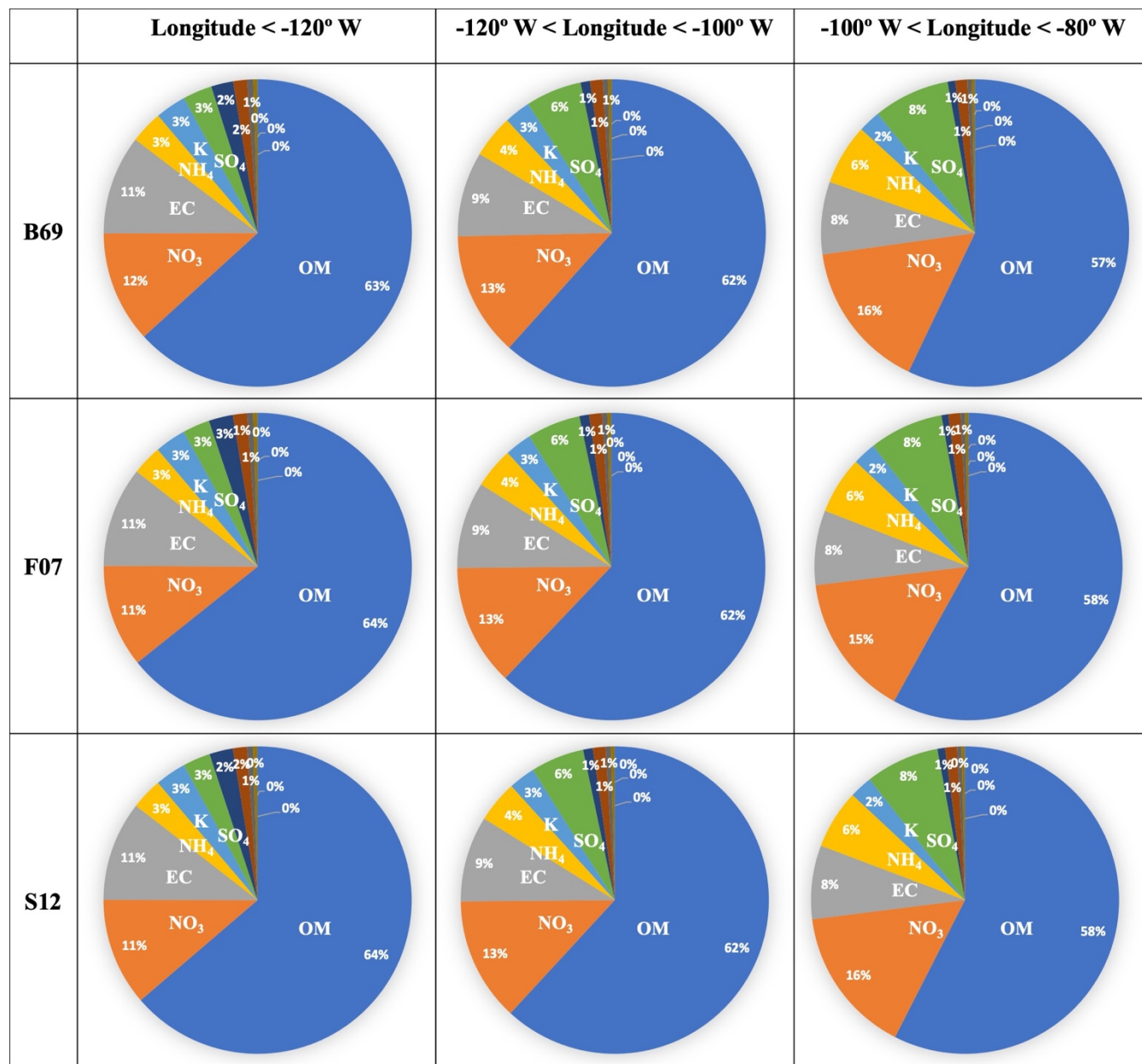
**Figure 3: Comparisons of net plume top heights (height minus terrain elevation) from three simulations: B69 (blue triangle), F07 (orange dot), and S12 (red rectangle), against aerosol height observations from the MISR aboard the Terra satellite (black dots) during the Milepost 21 fire on August 15<sup>th</sup>, 2020 (a) and the August Complex fire on August 31<sup>st</sup>, 2020 (b).**

220



### 3.2 Impact of estimated plume rise on PM<sub>2.5</sub> vertical distribution

In this section, we investigate the impact of plume injection height on different PM<sub>2.5</sub> components. Figure 4 shows the distribution of simulated fire emitted PM<sub>2.5</sub> components (the impact of other PM<sub>2.5</sub> sources was removed by subtracting the results of NoFire run) from B69, F07, and S12 in three different regions: the western U.S. (west of 120° W), Central U.S. (between 120° W and 100° W), and eastern U.S. (between 100° W and 80° W). For all three schemes, organic matter (OM) dominates the chemical composition of PM<sub>2.5</sub>, at 63%-64% near the source region in the western U.S., remains dominant in the downwind regions at ~ 61% between 120° W and 100° W, and 57% between 100° W and 80° W. A high OM portion highlights the predominant effect of wildfire emissions on air quality during the Gigafire period (Li et al., 2021). The second most abundant component is nitrate (NO<sub>3</sub>) at 11% - 12% near the source region and 13% - 16% in the downwind region. A higher portion of NO<sub>3</sub> in the downwind region than in the source region reflects the decreased contribution of OM and other primary aerosols, and increases in secondary aerosols, which include nitrate formation from both wildfires and anthropogenic emissions. The other component with a similar spatial gradient is ammonium (NH<sub>4</sub>), which contributes 3% to surface PM<sub>2.5</sub> near the source region and 5% - 6% in the downwind region. Elemental carbon contributes 10% to surface PM<sub>2.5</sub> concentration near the source region and 8% - 9% in the downwind region. Potassium (K), a fingerprint element to indicate fire contribution, accounts for 3% of surface PM<sub>2.5</sub> near the source region and 2% ~ 3% in the downwind region. Sulfate (SO<sub>4</sub>) contributed 3% near the source region and 6% - 8% in the downwind region. In summary, PM<sub>2.5</sub> species that are not significantly affected by secondary aerosol formation, such as elemental carbon and potassium, have their contributions decrease when transported downwind. For the PM<sub>2.5</sub> species that are affected by secondary aerosol formation (e.g., nitrate, sulfate, and ammonium), the contribution increases when transported downwind. These results show that the PM<sub>2.5</sub> composition, integrated over all vertical layers, is not sensitive to the choice of plume rise scheme.



■ Organic Matter   
 ■ Nitrate   
 ■ Elemental Carbon   
 ■ Ammonium   
 ■ Potassium   
 ■ Sulfate  
■ Chloride   
 ■ Soil   
 ■ Sodium   
 ■ Calcium   
 ■ Magnesium   
 ■ Hydronium Ion

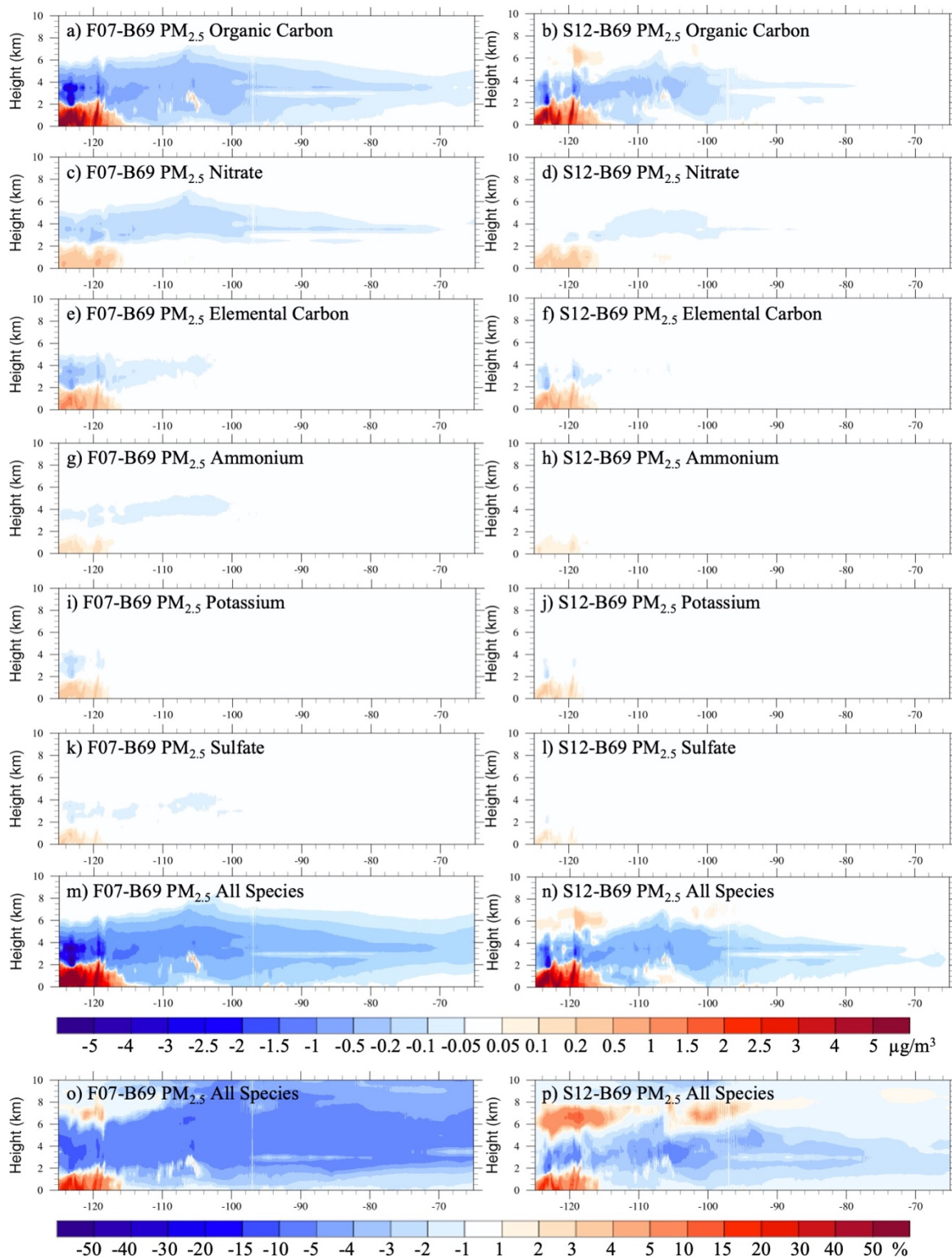
Figure 4: The simulated PM<sub>2.5</sub> chemical components (%) with the B69, F07, and S12 plume rise schemes in three different regions: in the west of 120° W (left), between 120° W and 100° W (middle), and between 100° W and 80° W (right). The data are integrated over all vertical layers, and averaged during the analysis period. The top 6 components are labeled in each plot.



Figure 5 shows the difference in the zonal mean concentrations of six major  $PM_{2.5}$  species (i.e., organic matter, nitrate, elemental carbon, ammonium, potassium, and sulfate) and total  $PM_{2.5}$  when using different plume rise schemes. Overall, most of the differences are found over the west coast region (longitude  $< -115^\circ$ ). The simulation with B69 produces a higher plume height on average, resulting in greater transport of smoke aloft, and hence higher downwind  $PM_{2.5}$  than that with the F07 or S12 schemes. The B69 plume rise scheme has a higher downwind impact and slightly lower near-source impact for  $PM_{2.5}$  species that contain secondary aerosols (e.g., organic matter, nitrate, ammonium, and sulfate) than primary aerosols (e.g., elemental carbon and potassium), due to the time required to form secondary aerosols.

255 Among the three simulations, the largest differences in  $PM_{2.5}$  are found from the surface to 8 km over the source region. Over the downwind region, the bulk of  $PM_{2.5}$  differences is found in the middle and upper troposphere. In addition, we noticed that the simulations with F07 and S12 produce more  $PM_{2.5}$  than that with B69 between 6-8 km during the analysis period. This is because, in the cases of a strong fire, the plume injection height simulated by F07 or S12 could be higher than B69 (e.g., Fig 2a). However, the difference in  $PM_{2.5}$  above 6 km is very small compared to those below 6 km. The total  $PM_{2.5}$  difference caused by different plume rise schemes is about 30% near the source and 5% in the downwind region. The difference in surface  $PM_{2.5}$  has a great impact on surface pollution levels and human health. More discussion on the impact of plume height on surface air quality is presented in section 3.4. Although the upper-level  $PM_{2.5}$  difference is expected to have a smaller impact on human health, it may affect cloud formation, photochemical reactions, and the radiative budget in the Earth system.

260





**Figure 5: (a-n) Zonal mean difference in predicted concentrations of six major PM<sub>2.5</sub> species among the simulations using the B69, F07, and S12 schemes from August 1<sup>st</sup> to September 30<sup>th</sup>, 2020: Organic Matter (a-b); Nitrate (c-d); Elemental Carbon (e-f); Ammonium (g-h); Potassium (i-j); and Sulfate (k-l). The difference in total PM<sub>2.5</sub> is displayed by both absolute values (m-n) and percentage (o-p).**

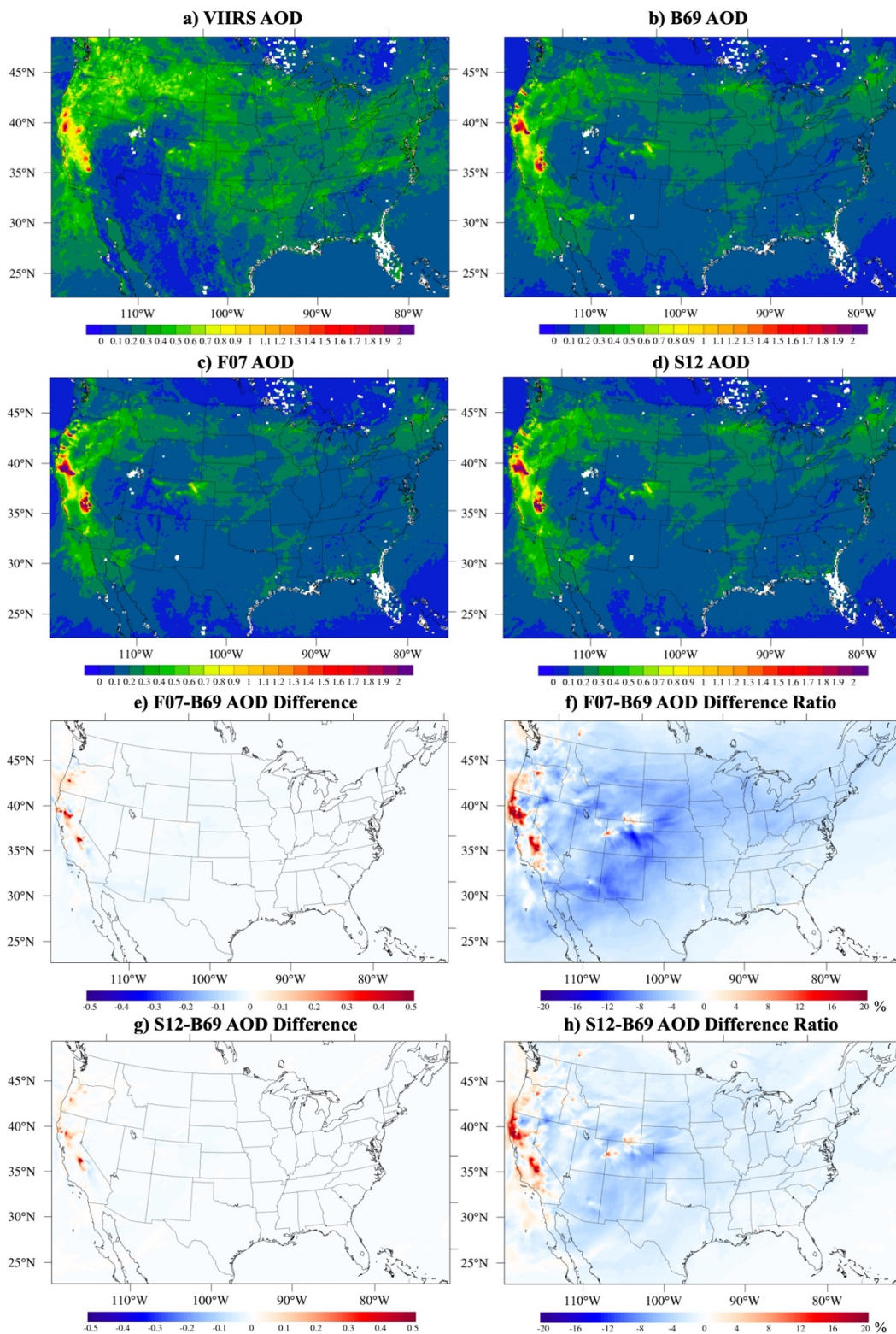
270

### **3.3 Impact of estimated plume rise on aerosol optical depth**

Wildfire smoke increases the aerosol loading in the atmosphere and consequently the AOD over both the source region and downwind regions. According to our previous study (Li et al., 2021), from September 14–17<sup>th</sup>, 2020 smoke from the West Coast was transported to the northeastern part of the U.S. The downwind transport of wildfire smoke is highly dependent on plume rise estimation. Figure 6 shows the two-month averaged AOD from VIIRS (Figure 6a) compared with model simulations (Figures 6b-d), and the AOD differences and the difference ratio (percentage of the difference to B69) in the different plume rise scheme simulations (Figures 6e-h). Near the source region, F07 and S12 simulate more AOD than B69, a pattern that is the opposite of that for plume rise estimation (lower plume height than that with B69). In the downwind region, B69 simulates more AOD than F07 and S12. The difference is approximately 20-30% over the source region and 5-10% over the downwind region.

280

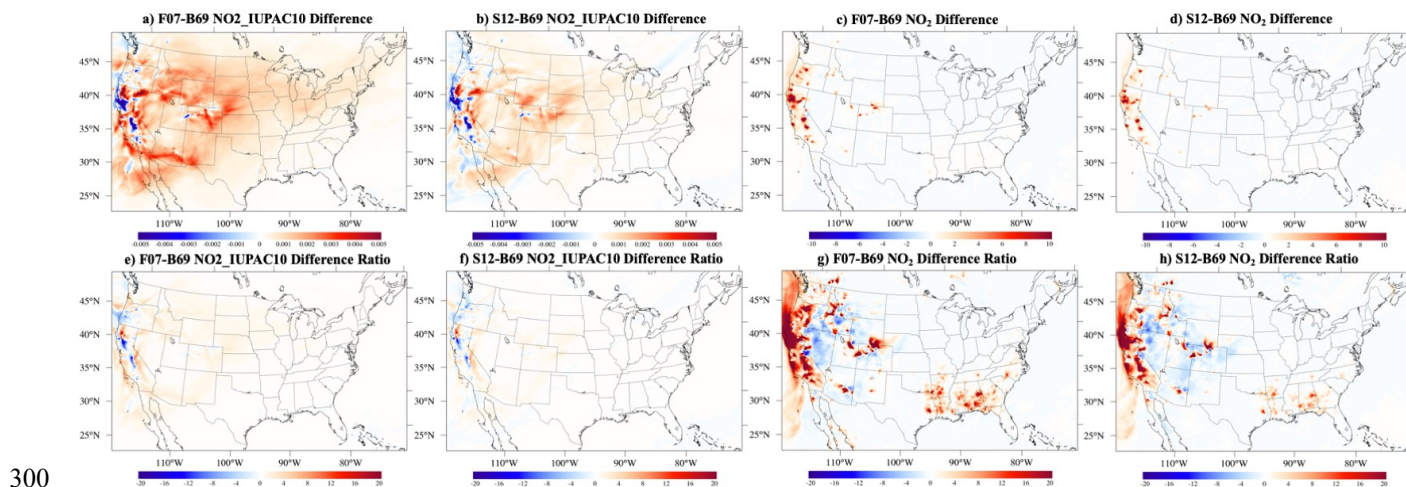






285 **Figure 6: Two-month averaged AOD from VIIRS (a), B69 run (b), F07 run (c), and S12 run (d); e) The averaged AOD differences between CMAQ simulations with the Freitas 2007 (F07) and Briggs 1969 (B69) plume rise schemes from August 1<sup>st</sup>, 2020 to September 30<sup>th</sup>, 2020; f) the averaged AOD difference ratio between F07 and B69 during the same period; g) same as e) but between Sofiev 2012 (S12) and B69; h) same as f) but for S12 and B69.**

Next, we examine how the altered optical depth affects photochemistry. The thicker smoke, indicated by higher AOD, may absorb and/or scatter a larger fraction of sunlight, hence affecting photolysis reactions (Dickerson et al., 1997; Castro et al., 2001; Kumar et al., 2014; Baylon et al., 2018). Here we focus on the photolysis rate of NO<sub>2</sub> ( $\text{NO}_2 + h\nu \rightarrow \text{NO} + \text{O}$ ), which is a key reaction that leads to the formation of tropospheric ozone. The difference between NO<sub>2</sub> photolysis rate (NO<sub>2</sub>\_IUPAC10, in min<sup>-1</sup>) and NO<sub>2</sub> (ppbV) are shown in Figure 7. Near the source region where F07 and S12 simulate a higher AOD, the NO<sub>2</sub>\_IUPAC10 is reduced (Figure 7 a, b, e, and f), which means that the thick wildfire smoke decreases the photolysis rate for the reaction NO<sub>2</sub>→NO+O. The change in the NO<sub>2</sub>\_IUPAC10 would also affect NO<sub>2</sub> concentrations. According to Figure 7 c, d, g, and h, the NO<sub>2</sub> concentrations from F07 and S12 are higher than B69 in the source region, where F07 and S12 simulate a higher AOD. However, if we compare the difference ratio for AOD with NO<sub>2</sub>, the NO<sub>2</sub> difference ratio near the source region is higher than AOD. This suggests that the difference in NO<sub>2</sub> is not solely caused by wildfire emission or dispersion. The reduced photolysis rate (NO<sub>2</sub>\_IUPAC10) is one of the reasons for this strengthened NO<sub>2</sub> increase, because less NO<sub>2</sub> is converted to NO. The consumption of NO<sub>2</sub> is slowed down so that the NO<sub>2</sub> concentration is higher in the high AOD area.



300 **Figure 7: Same as Figure 5, but for photolysis rate NO<sub>2</sub>\_IUPAC10 and NO<sub>2</sub>.**

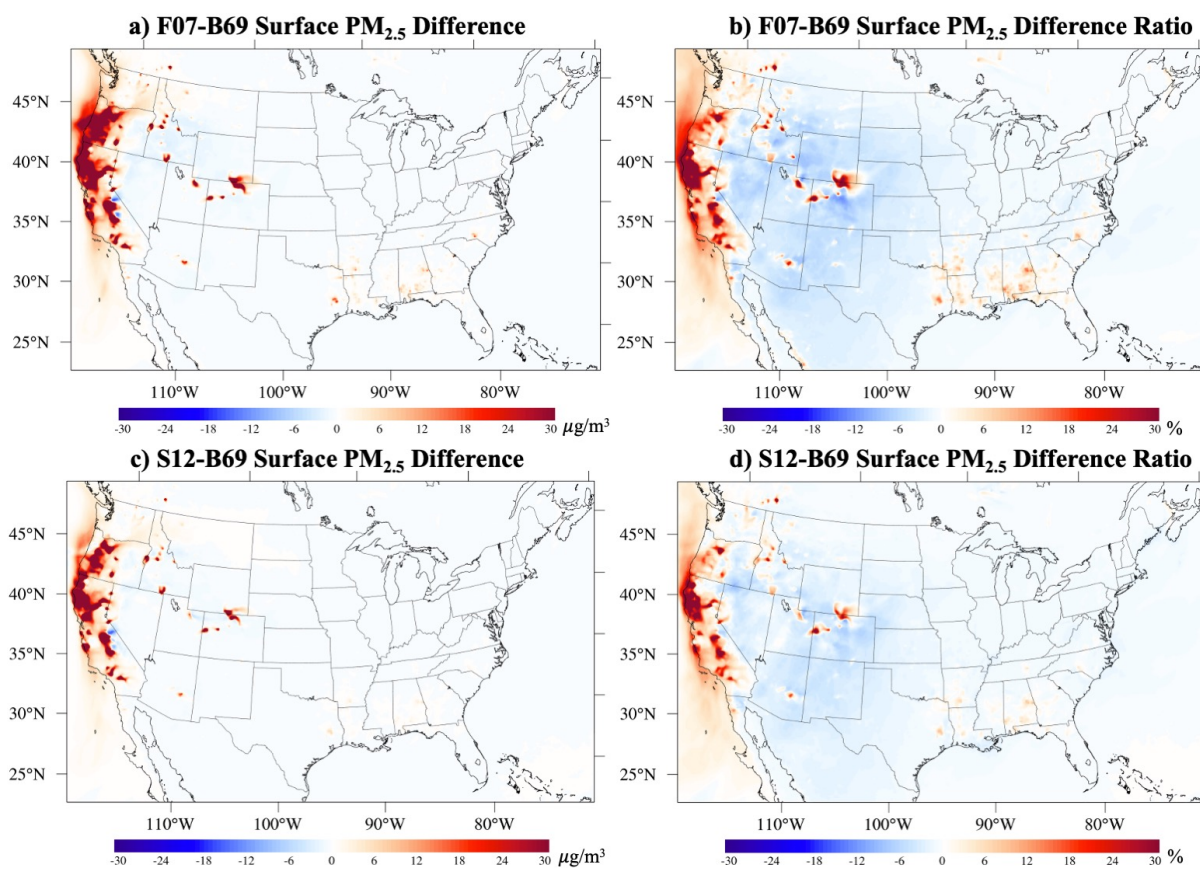
### 3.4 Impact of estimated plume rise on surface PM<sub>2.5</sub> and exceedance of NAAQS

Surface or ambient PM<sub>2.5</sub> is the common measure used to link exposure to wildfire smoke to health endpoints such as asthma and chronic obstructive pulmonary disease (Reid et al., 2016). To protect human health and the environment, the National





305 Ambient Air Quality Standards (NAAQS) have been established for PM<sub>2.5</sub> and other criteria air pollutants (NO<sub>2</sub>, O<sub>3</sub>, SO<sub>2</sub>, CO, PM<sub>10</sub>, and lead). The daily PM<sub>2.5</sub> NAAQS is 35  $\mu\text{g}/\text{m}^3$  for the 24-hour mean PM<sub>2.5</sub> concentration (U.S. EPA, 2020c). The simulated surface PM<sub>2.5</sub> differences caused by different plume rise schemes are shown in Figure 8. The F07 and S12 simulations, which have averaged lower initial plume heights, yield higher surface PM<sub>2.5</sub> concentrations than the B69 simulation over the west coast, whereas the opposite patterns are found in the central and the eastern U.S. The surface PM<sub>2.5</sub> difference caused by different plume rise schemes reaches 70% over the west coast, which is much higher than the AOD  
310 difference caused by different plume rise schemes reaches 70% over the west coast, which is much higher than the AOD differences. In the downwind regions, the surface PM<sub>2.5</sub> difference caused by different plume rise schemes is less than 15%, meaning that the effects of the plume rise estimation on surface PM<sub>2.5</sub> occur mainly near the source region.



315 **Figure 8:** a) The averaged surface PM<sub>2.5</sub> differences between F07 and B69 from August 1<sup>st</sup>, 2020, to September 30<sup>th</sup>, 2020; b) the averaged surface PM<sub>2.5</sub> difference ratio between F07 and B69 during the same period; c) same as a) but between S12 and B69; d) same as b) but between S12 and B69.

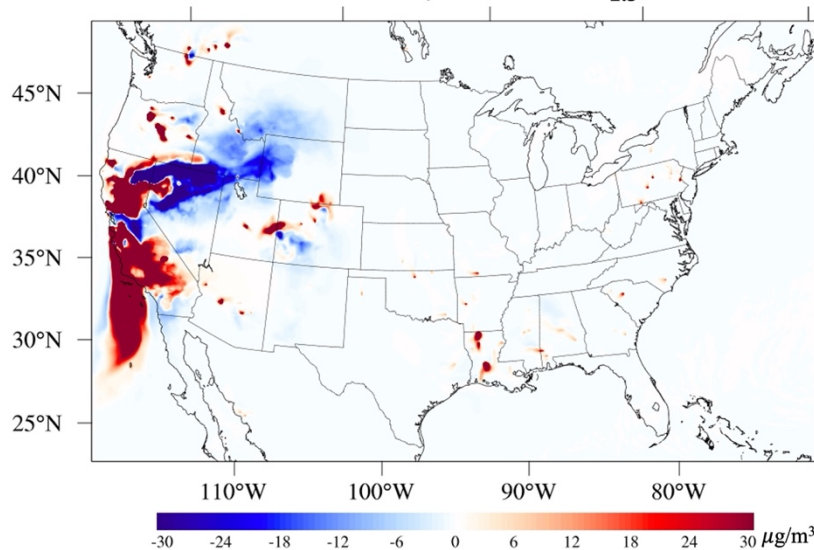
Next, we will examine how the plume rise estimation affects the prediction of PM<sub>2.5</sub> exceedances. Figure 9a shows the daily  
320 mean surface PM<sub>2.5</sub> difference between the F07 and B69 runs for Aug 20<sup>th</sup>, 2020. The simulated PM<sub>2.5</sub> exceedance regions by



different plume rise schemes are overlaid by AirNow observed exceedance for the same day (Figure 9b). The brown color represents the region where the runs with all three schemes simulate  $PM_{2.5}$  exceedances; the blue (red/yellow) color represents the region where only B69 (S12/F07) simulates the  $PM_{2.5}$  exceedance; the green represents the region where both the B69 and F07 simulate the  $PM_{2.5}$  exceedance; the magenta color represents the region where both the B69 and S12 simulate the  $PM_{2.5}$  exceedance; the orange represents the region where both F07 and S12 simulate the  $PM_{2.5}$  exceedance. According to Figure 9b, on August 20<sup>th</sup>, 2020, B69 and S12 simulated more  $PM_{2.5}$  exceedance in the downwind regions (Wyoming (WY) and Idaho (ID)), whereas F07 and S12 simulated more exceedance in the southeastern U.S., where prescribed fires were the major biomass burning sources. In WY and ID, where F07 did not simulate the  $PM_{2.5}$  exceedance whereas B69 and S12 did, the difference between F07 and B69 reached  $15 \mu\text{g}/\text{m}^3$  (Figure 9a). Although these schemes agree on the  $PM_{2.5}$  exceedance forecast in the majority region, the disagreements in the downwind region (i.e., ID and WY for this case) may affect key decision-making on early warnings of extreme air pollution episodes at local levels during large wildfire events.



**a) 20200820 F07-B69 daily surface  $PM_{2.5}$  difference**



**b) Simulated  $PM_{2.5}$  exceedance regions by B69, F07 & S12 compared with AirNow observation**

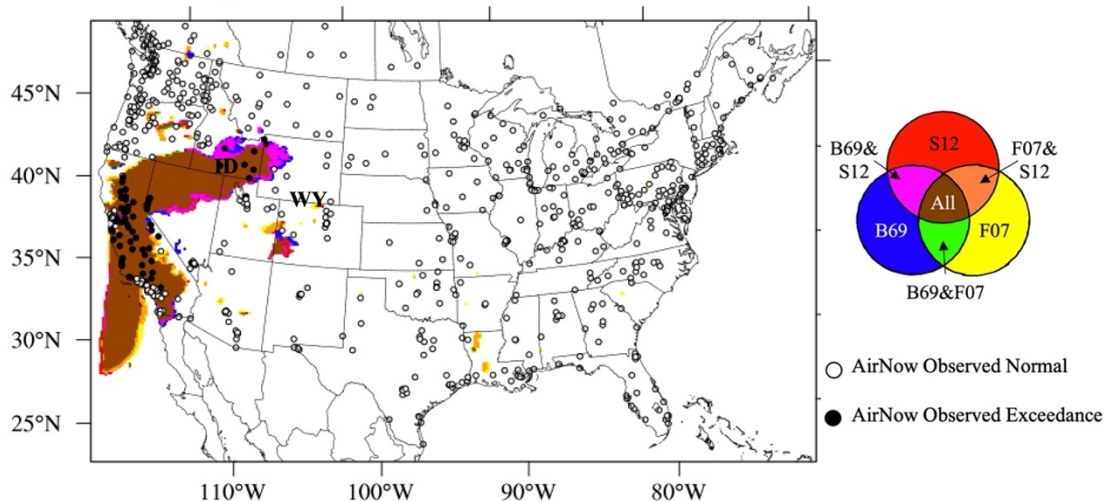


Figure 9: a) The daily mean surface  $PM_{2.5}$  difference between F07 and B69 runs for August 20<sup>th</sup>, 2020; b) simulated  $PM_{2.5}$  exceedance regions by B69, F07, and S12 overlaid by AirNow observed exceedance for August 20<sup>th</sup>, 2020. The brown color represents the region where the runs with all three schemes simulate  $PM_{2.5}$  exceedances; the blue (red/yellow) color represents the region where only B69 (S12/F07) simulates the  $PM_{2.5}$  exceedance; the green represents the region where both the B69 and F07 simulate the  $PM_{2.5}$  exceedance; the magenta color represents the region where both the B69 and S12 simulate the  $PM_{2.5}$  exceedance; the orange represents the region where both F07 and S12 simulate the  $PM_{2.5}$  exceedance.

335



#### 340 4 Conclusion

In this study, we use CMAQ with three different plume rise schemes, namely Briggs 1969 (B69), Freitas 2007 (F07), and Sofiev 2012 (S12), to understand the impact of plume rise calculation on aerosol and photochemistry during the 2020 western U.S. wildfire season. The simulated plume heights by all three schemes are comparable to MISR observations of aerosol height. The performance of the simulations with different schemes varies for different fire cases and weather conditions (i.e.,  
345 humidity). On average, the B69 predicts a higher injection height than F07 and S12, and leads to higher downwind PM<sub>2.5</sub> concentrations due to the stronger transport at a higher altitude. The largest PM<sub>2.5</sub> differences are found from the surface to 8 km over the source region. Over the downwind region, the bulk of the PM<sub>2.5</sub> differences is found in the middle and upper troposphere. The total PM<sub>2.5</sub> difference is approximately 30% near the source and 5% in the downwind region. Furthermore, we found that the plume rise scheme has a higher downwind impact and slightly lower near-source impact for PM<sub>2.5</sub> species  
350 that contain secondary aerosols over primary aerosols.

Thick fire smoke also increases AOD in the source and the downwind regions. On average, F07 and S12, which estimate lower plume height, simulate greater smoke AOD near the fire source region than B69. In the downwind region, B69 simulates higher AOD than F07 and S12. The difference is approximately 20-30% near the source region and 5-10% in the downwind  
355 region. When AOD is higher, the thicker smoke may block more sunlight and affect the photolysis reaction rates. Near the source region, where F07 and S12 simulate a higher AOD, the photolysis reaction rate decreases, resulting in higher NO<sub>2</sub> concentrations. The rate of change of NO<sub>2</sub> is higher than that of AOD, which suggests that the difference in NO<sub>2</sub> is not only caused by wildfire emission or dispersion, but also by the reduced photolysis rate.

360 Finally, we analyzed the effect of plume rise estimation on the prediction of PM<sub>2.5</sub> exceedances. The F07 and S12 simulations, which have averaged lower plume heights, predict higher surface PM<sub>2.5</sub> concentrations than B69 over the west coast, whereas the opposite patterns are found in the central and the eastern U.S. The effects of the plume rise estimation on surface PM<sub>2.5</sub> occur mainly near the source region. The surface PM<sub>2.5</sub> difference caused by different plume rise schemes reaches 70% over the west coast and is less than 15% in the downwind regions. These results suggest that the effects of plume rise estimation on  
365 surface PM<sub>2.5</sub> occur mainly near the source region, whereas in the downwind region, the majority of effects are in the free troposphere. For PM<sub>2.5</sub> exceedance prediction, higher plume height produces a larger PM<sub>2.5</sub> exceedance area in the downwind region. In most affected areas, the predicted PM<sub>2.5</sub> exceedance regions from the three schemes overlapped. In non-overlapping regions, the simulated differences in PM<sub>2.5</sub> could reach 15 µg/m<sup>3</sup>. Such PM<sub>2.5</sub> exceedance forecast differences may affect key decision-making on early warnings of extreme air pollution episodes at local levels during large wildfire events.

370

The analysis concerning the impact of the plume rise scheme on NO<sub>2</sub> is only qualitative. More quantitative analysis using CMAQ process analysis will be discussed in a subsequent paper. Moreover, the WRF-CMAQ system used in this study is an





375 offline model. The heat emitted by the fire calculated in the CMAQ does not influence the meteorology model (WRF), such as the PBL height, temperature and wind field. In the future, online models will be utilized to further study the plume rise estimation impacts on air quality.

*Code availability.* CMAQ documentation and released versions of the source code are available on the U.S. EPA modeling site <https://www.cmascenter.org/>. The source code of WRF is available at <https://github.com/wrf-model/WRF>.

380 *Data availability.* The MISR data used in this paper can be found here: [http://air.csiss.gmu.edu/yli/paper\\_data/MISR](http://air.csiss.gmu.edu/yli/paper_data/MISR). The GBBEPx data can be downloaded from <https://satepsanone.nesdis.noaa.gov/pub/FIRE/GBBEPx-V3/>. The VIIRS measurements can be downloaded from [http://air.csiss.gmu.edu/yli/paper\\_data/viirs/](http://air.csiss.gmu.edu/yli/paper_data/viirs/). The AirNow observations can be downloaded from: <https://files.airnowtech.org/?prefix=airnow/2020/>. The CMAQ results can be download from: [http://air.csiss.gmu.edu/yli/paper\\_data/](http://air.csiss.gmu.edu/yli/paper_data/).

385 *Competing interests.* The authors declare that they have no conflict of interest.

*Author contributions.* YL and DT designed the study and performed the research with contributions from all co-authors. SF, RA, MS, and GG prepared plume rise code. SM, XZ, SK, and FL prepared fire emission data. RK prepared the MISR data and 390 guided the evaluation of plume height estimation. YL and DT wrote and revised the paper, with input from YT, BB, and PC. All authors commented on drafts of the paper.

*Acknowledgments.* This work was financially supported by the NASA Health and Air Quality Program, NOAA Weather Program Office, and George Mason University College of Science. The observation data from NASA, NOAA and US EPA 395 are gratefully acknowledged.

## References

- Ahmadov, R., Grell, G., James, E., Csiszar, I., Tsidulko, M., Pierce, B., et al.: Using VIIRS Fire Radiative Power data to simulate biomass burning emissions, plume rise and smoke transport in a real-time air quality modeling system. Ieee International Geoscience and Remote Sensing Symposium. IEEE International Symposium on Geoscience and Remote 400 Sensing IGARSS. New York: Ieee; 2017. p. 2806-8, 2017
- Akagi, S. K., Yokelson, R. J., Burling, I. R., Meinardi, S., Simpson, I., Blake, D. R., McMeeking, G. R., Sullivan, A., Lee, T., Kreidenweis, S., Urbanski, S., Reardon, J., Griffith, D. W. T., Johnson, T. J., and Weise, D. R.: Measurements of reactive trace gases and variable O<sub>3</sub> formation rates in some South Carolina biomass burning plumes, Atmos. Chem. Phys., 13, 1141–1165, <https://doi.org/10.5194/acp-13-1141-2013>, 2013.



- 405 Archer-Nicholls, S., Lowe, D., Darbyshire, E., Morgan, W. T., Bela, M. M., Pereira, G., Trembath, J., Kaiser, J. W., Longo, K. M., Freitas, S. R., Coe, H., and McFiggans, G.: Characterising Brazilian biomass burning emissions using WRF-Chem with MOSAIC sectional aerosol, *Geosci. Model Dev.*, 8, 549–577, <https://doi.org/10.5194/gmd-8-549-2015>, 2015.
- Baylon, P., Jaffe, D. A., Hall, S. R., Ullmann, K., Alvarado, M. J., and Lefer, B. L.: Impact of biomass burning plumes on photolysis rates and ozone formation at the Mount Bachelor Observatory. *Journal of Geophysical Research: Atmospheres*, 410 123, 2272–2284. <https://doi.org/10.1002/2017JD027341>, 2018
- Briggs, G. A.: Plume rise, *Tech. Rep. Crit. Rev. Ser. 81pp.*, Natl. Tech. Inf. Serv., Springfield, VA, 1969.
- Briggs, G. A.: Some recent analyses of plume rise observations. *Proceedings of the Second International Clean Air Congress*, H. M. Englund and W. T. Beery, Eds., Academic Press, New York, 1029–1032, 1971.
- Briggs, G. A.: Discussion on chimney plumes in neutral and stable surroundings. *Atmos. Environ.*, 6, 507–510, 1972.
- 415 Byun, D. W., & Schere, K. L. (2006). Review of the governing equations, computational algorithms, and other components of the models-3 community multiscale air quality (CMAQ) modeling system. *Applied Mechanics Reviews*, 59, 51–77. <http://dx.doi.org/10.1115/1.2128636>
- Castro, T. Madronich, S., Rivale, S., Muhlia, A., and Mar, B.: The influence of aerosols on photochemical smog in Mexico City, *Atmos. Environ.*, 35, 1765–1772, 2001.
- 420 Cascio WE.: Wildland fire smoke and human health. *Sci Total Environ.* doi: 10.1016/j.scitotenv.2017.12.086, 2018.
- Dickerson, R. R., Kondragunta, S., Stenchikov, G., Civerolo, K. L., Doddridge, B. G., and Holben, B. N.: The impact of aerosols on solar ultraviolet radiation and photochemical smog. *Science*, 278(5339), 827–830. DOI: 10.1126/science.278.5339.827, 1997.
- Draxler, R.R. and Hess, G.D.: An Overview of the HYSPLIT4 Modeling System of Trajectories, Dispersion, and Deposition. *Australian Meteorological Magazine*, 47, 295–308, 1998.
- 425 Diner, D.J., Beckert, J.C., Reilly, T.H., Bruegge, C.J., Conel, J.E., Kahn, R.A., Martonchik, J.V., Ackerman, T.P., Davies, R., Gerstl, S.A., et al.: Multi-angle Imaging SpectroRadiometer (MISR) instrument description and experiment overview. *IEEE Trans. Geosci. Remote Sens.* 1998, 36, 1072–1087, 1998.
- Eyth, A., Vukovich, J., Farkas, C., & Strum, M.: Technical Support Document (TSD) Preparation of Emissions Inventories for 2016v1 North American Emissions Modeling Platform, 2020.
- 430 Fahey, K.M., Carlton, A.G., Pye, H.O.T., Baek, J., Hutzell, W.T., Stanier, C.O., Baker, K.R., Appel, K.W., Jaoui, M., & Offenberg, J.H.: A framework for expanding aqueous chemistry in the Community Multiscale Air Quality (CMAQ) model version 5.1. *Geoscientific Model Development*, 10, 1587–1605. doi: 10.5194/gmd-10-1587-2017, 2017.
- Freitas, S. R., Longo, K. M., Chatfield, R., Latham, D., Silva Dias, M. A. F., Andreae, M. O., Prins, E., Santos, J. C., Gielow, R., & Carvalho, J. A. Jr.: Including the sub-grid scale plume rise of vegetation fires in low resolution atmospheric transport models. *Atmospheric Chemistry and Physics*, 7(13), 3385–3398. <https://doi.org/10.5194/acp-7-3385-2007>, 2007.
- 435 Grell, G. A., & Freitas, S. R.: A scale and aerosol aware stochastic convective parameterization for weather and air quality modeling. *Atmospheric Chemistry and Physics*, 14(10), 5233–5250. <https://doi.org/10.5194/acp-14-5233-2014>, 2014.



- Houyoux, M., Vukovich, J., Brandmeyer, J. E., Seppanen, C., & Holland, A.: Sparse matrix operator kernel emissions modeling system-SMOKE User manual. Prepared by MCNC-North Carolina Supercomputing Center, Environmental Programs, Research Triangle Park, NC, 2000.
- Iacono, M. J., Delamere, J. S., Mlawer, E. J., Shephard, M. W., Clough, S. A., & Collins, W. D.: Radiative forcing by long-lived greenhouse gases: Calculations with the AER radiative transfer models. *Journal of Geophysical Research*, 113, D13103. <https://doi.org/10.1029/2008JD009944>, 2008.
- 445 Janjić, Z. I.: The Step-Mountain Eta Coordinate Model: Further developments of the convection, viscous sublayer, and turbulence closure schemes. *Monthly Weather Review*, 122(5), 927–945. [https://doi.org/10.1175/1520-0493\(1994\)122<0927:TSMECM>2.0.CO;2](https://doi.org/10.1175/1520-0493(1994)122<0927:TSMECM>2.0.CO;2), 1994.
- Johnston, F., Henderson, S., Chen, Y., Randerson, J., Marlier, M., DeFries, R., et al.: Estimated Global Mortality Attributable to Smoke from Landscape Fires. *Environ Health Perspect.* 2012 May; 120(5): 695–701. doi: 10.1289/ehp.1104422, 2012.
- 450 Koning, H. W., Smith, K. R., & Last, J. M.: Biomass fuel combustion and health, *Bulletin of the World Health Organization*, 63 (1), 11-26, 1985.
- Koren, V., Schaake, J., Mitchell, K., Duan, Q.-Y., Chen, F., & Baker, J. M.: A parameterization of snowpack and frozen ground intended for NCEP weather and climate models. *Journal of Geophysical Research*, 104, 19,569–19,585. <https://doi.org/10.1029/1999JD900232>, 1999.
- 455 Kumar, R., Barth, M. C., Madronich, S., Naja, M., Carmichael, G. R., Pfister, G. G., Knote, C., Brasseur, G. P., Ojha, N., and Sarangi, T.: Effects of dust aerosols on tropospheric chemistry during a typical pre-monsoon season dust storm in northern India, *Atmos. Chem. Phys.*, 14, 6813–6834, <https://doi.org/10.5194/acp-14-6813-2014>, 2014.
- Li, Y., Tong, D. Q., Ngan, F., Cohen, M. D., Stein, A. F., Kondragunta, S., et al.: Ensemble PM<sub>2.5</sub> forecasting during the 2018 Camp Fire event using the HYSPLIT transport and dispersion model. *J. Geophys. Res. Atmos: Atmospheres*, 125, e2020JD032768. <https://doi.org/10.1029/2020JD032768>, 2020.
- 460 Li, Y., Tong, D., Ma, S., Zhang, X., Kondragunta, S., Li, F., & Saylor, R.: Dominance of wildfires impact on air quality exceedances during the 2020 record-breaking wildfire season in the United States. *Geophysical Research Letters*, 48, e2021GL094908. <https://doi.org/10.1029/2021GL094908>, 2021.
- Liu, Y., Austin, E., Xiang, J., Gould, T., Larson, T., & Seto, E.: Health impact assessment of the 2020 Washington State wildfire smoke episode: Excess health burden attributable to increased PM<sub>2.5</sub> exposures and potential exposure reductions. *GeoHealth*, 5, e2020GH000359. <https://doi.org/10.1029/2020GH000359>, 2021.
- 465 Luecken, D.J., Yarwood, G., & Hutzell, W.H.: Multipollutant of ozone, reactive nitrogen and HAPs across the continental US with CMAQ-CB6. *Atmospheric Environment*, 201, 62-72. doi: 10.1016/j.atmosenv.2018.11.060, 2019.
- Morrison, H., Thompson, G., & Tatarskii, V.: Impact of cloud microphysics on the development of trailing Stratiform precipitation in a simulated squall line: Comparison of one- and two-moment schemes. *Monthly Weather Review*, 137(3), 991–1007. <https://doi.org/10.1175/2008MWR2556.1>, 2019.
- 470



- Nelson, D.L., Garay, M.J., Kahn, R.A., and Dunst, B.A.: Stereoscopic Height and Wind Retrievals for Aerosol Plumes with the MISR INteractive eXplorer (MINX). *Remote Sens.* 5, 4593-4628, doi:10.3390/rs5094593, 2013.
- 475 O'Neill, S. M., Diao, M., Raffuse, S., Al-Hamdan, M., Barik, M., Jia, Y., Reid, S., et al.: A multi-analysis approach for estimating regional health impacts from the 2017 Northern California wildfires, *Journal of the Air & Waste Management Association*, 71:7, 791-814, DOI: 10.1080/10962247.2021.1891994, 2021.
- Pye, H.O.T., Luecken, D.J., Xu, L., Boyd, C.M, Ng, N.L., Baker, K.R., Ayres, B.R., Bash, J.O., Baumann, K., Carter, W. P.L., Edgerton, E., Fry, J.L., Hutzell, W.T., Schwede, D.B., Shepson, P.B.: Modeling the current and future roles of particulate organic nitrates in the southeastern United States. *Environ Sci Technol* 2015, 49(24), 14195-14203. doi:  
480 10.1021/acs.est.5b03738, 2015.
- Reid, C.E., Brauer, M., Johnston, F.H., Jerrett, M., Balmes, J.R., Elliott, C.T.: Critical review of health impacts of wildfire smoke exposure. *Environ. Health Perspect.* 124, 1334–1343, 2016.
- Skamarock, W. C., J. B. Klemp, J. Dudhia, D. O. Gill, Z. Liu, J. Berner, W. Wang, J. G. Powers, M. G. Duda, D. M. Barker, and X.-Y. Huang: A Description of the Advanced Research WRF Version 4. NCAR Tech. Note NCAR/TN-556+STR, 145  
485 pp, doi:10.5065/1dfh-6p97, 2019.
- Sofiev, M., Ermakova, T., & Vankevich, R.: Evaluation of the smoke-injection height from wild-land fires using remote-sensing data. *Atmospheric Chemistry and Physics*, 12(4), 1995–2006. <https://doi.org/10.5194/acp-12-1995-2012>, 2012.
- Tang, Y., G. R. Carmichael, I. Uno, J.-H. Woo, G. Kurata, B. Lefer, R. E. Shetter, H. Huang, B. E. Anderson, M. A. Avery, A. D. Clarke and D. R. Blake, Impacts of aerosols and clouds on photolysis frequencies and photochemistry during TRACE-  
490 P, part II: three-dimensional study using a regional chemical transport model, *Journal of Geophysical Research*, 108(D21), 8822, doi:10.1029/2002JD003100, 2003.
- United States Environmental Protection Agency: CMAQ (Version 5.3.2) [Software]. Available from <https://doi.org/10.5281/zenodo.4081737>, 2020a.
- United States Environmental Protection Agency: Technical Support Document (TSD) Preparation of Emissions Inventories  
495 for 2016v1 North American Emissions Modeling Platform, section 3.3, p120-121. Available at: [https://www.epa.gov/sites/default/files/2020-10/documents/2016v1\\_emismod\\_tsd\\_508.pdf](https://www.epa.gov/sites/default/files/2020-10/documents/2016v1_emismod_tsd_508.pdf), 2020b.
- United States Environmental Protection Agency: Review of the National Ambient Air Quality Standards for Particulate Matter. *Federal Register*, 85, December 18, 2020, 82684-82748. Available at: <https://www.govinfo.gov/content/pkg/FR-2020-12-18/pdf/2020-27125.pdf>, 2020c.
- 500 Val Martín, M. V., Honrath, R. E., Owen, R. C., Pfister, G., Fialho, P., & Barata, F.: Significant enhancements of nitrogen oxides, black carbon, and ozone in the North Atlantic lower free troposphere resulting from North American boreal wildfires, *Journal of Geophysical Research: Atmospheres*, 111(D23), <https://doi.org/10.1029/2006JD007530>, 2006.
- Val Martin, M., Logan, J.A., Kahn, R.A., Leung, F.-Y., Nelson, D., and Diner, D.: Smoke injection heights from fires in North America: analysis of 5 years of satellite observations. *Atm. Chem. Phys.* 10, 1491-1510, doi: 10.5194/ACP-10-1491-2010,  
505 2010.



- Val Martin, M., Kahn, R. A., Logan, J. A., Paugam, R., Wooster, M., & Ichoku, C.: Space-based observational constraints for 1-D fire smoke plume-rise models. *Journal of Geophysical Research*, 117, D22204. <https://doi.org/10.1029/2012JD018370>, 2012.
- Val Martin, M., Kahn, R. A., and Tosca, M. G.: A Global Analysis of Wildfire Smoke Injection Heights Derived from Space-  
510 Based Multi-Angle Imaging. *Remote Sensing*, 2018, 10, 1609; doi:10.3390/rs1010, 2018.
- Vernon, C.J., Bolt, R., Canty, T., and Kahn, R.A.: The impact of MISR-derived injection-height initialization on wildfire and volcanic plume dispersion in the HySPLIT model. *Atmosph. Meas. Tech.* 11, 6289–6307, doi: 10.5194/amt-11-6289-2018, 2018
- Xu, L., Pye, H. O. T., He, J., Chen, Y. L., Murphy, B. N., Ng, N. L.: Experimental and model estimates of the contributions  
515 from biogenic monoterpenes and sesquiterpenes to secondary organic aerosol in the southeastern United States. *Atmos. Chem. Phys.*, 18: 12613-12637. doi: 10.5194/acp-18-12613-2018, 2018.
- Ye, X., Arab, P., Ahmadov, R., James, E., Grell, G. A., Pierce, B., Kumar, A., Makar, P., Chen, J., Davignon, D., Carmichael, G. R., Ferrada, G., McQueen, J., Huang, J., Kumar, R., Emmons, L., Herron-Thorpe, F. L., Parrington, M., Engelen, R., Peuch, V.-H., da Silva, A., Soja, A., Gargulinski, E., Wiggins, E., Hair, J. W., Fenn, M., Shingler, T., Kondragunta, S., Lyapustin, A.,  
520 Wang, Y., Holben, B., Giles, D. M., and Saide, P. E.: Evaluation and intercomparison of wildfire smoke forecasts from multiple modeling systems for the 2019 Williams Flats fire, *Atmos. Chem. Phys.*, 21, 14427–14469, <https://doi.org/10.5194/acp-21-14427-2021>, 2021.
- Zhang, X., Kondragunta, S., Da Silva, A., Lu, S., Ding, H., Li, F., & Zhu, Y.: The blended global biomass burning emissions product from MODIS and VIIRS observations (GBBEPx) version 3.1,  
525 [https://www.ospo.noaa.gov/Products/land/gbbepx/docs/GBBEPx\\_ATBD.pdf](https://www.ospo.noaa.gov/Products/land/gbbepx/docs/GBBEPx_ATBD.pdf), 2019.
- Zhang, X., Kondragunta, S., Ram, J., Schmidt, C., & Huang, H.-C.: Near-real-time global biomass burning emissions product from geostationary satellite constellation. *Journal of Geophysical Research: Atmospheres*, 117(D14). <https://doi.org/10.1029/2012JD017459>, 2012.